scientific reports

Check for updates

OPEN

Contrast-enhanced magnetic resonance neurography for diagnosing brachial plexopathy: improved visualization and additional imaging features

Wenjun Wu[1,2]✉, Yuhong Ding[3], Yu Su[1], Youzhi Wang[1], Tingting Liu[1], Dingxi Liu[1,2], Chungao Li[1,2], Chuansheng Zheng[1,2], Lixia Wang[1,2] & Xi Long[1,2]✉

Contrast-enhanced magnetic resonance neurography (CE-MRN) holds promise for diagnosing brachial plexopathy by enhancing nerve visualization and revealing additional imaging features in various lesions. This study aims to validate CE-MRN's efficacy in improving brachial plexus (BP) imaging across different patient cohorts. Seventy-one subjects, including 19 volunteers and 52 patients with BP compression/entrapment, injury, and neoplasms, underwent both CE-MRN and plain MRN. Two radiologists assessed nerve visibility, with inter-reader agreement evaluated. Quantitative parameters such as signal intensity (SI), contrast-to-noise ratio (CNR), and contrast ratio (CR) of the C7 nerve were measured. Both qualitative scoring and quantitative metrics were compared between CE-MRN and plain MRN within each patient group. Patient classification followed the Neuropathy Score Reporting and Data System (NS-RADS), summarizing additional imaging features for each brachial plexopathy type. Inter-reader agreement for qualitative assessment was strong. CE-MRN significantly enhanced BP visualization and nerve-tissue contrast across all cohorts, particularly in volunteers and patients with injuries. It also uncovered additional imaging features such as hypointense signals in ganglia, compressed nerve sites, and neoplastic enhancements. CE-MRN effectively mitigated muscle edema and vascular contamination, enabling precise classification of BP injuries. Overall, CE-MRN consistently enhances BP visualization and provides valuable imaging features for accurate diagnosis.

Keywords Magnetic resonance imaging, Contrast-enhanced magnetic resonance neurography, Brachial plexus, Brachial plexopathy, Neuropathy score reporting and data system

Magnetic resonance neurography (MRN) has emerged as a prominent imaging modality for the visualization and diagnosis of brachial plexus (BP). To address the imaging challenges posed by the morphological complexity of BP, a wide range of MR sequences and techniques have been developed, including advanced high-resolution 2D or 3D sequences as well as various fat and vascular suppression techniques[1,2]. Due to the diverse etiology of brachial plexopathy, not only does signal contamination from normal tissues such as fat, vasculature, musculature, and lymph nodes impede high-quality MRN, but also muscle edema, mass effect and denervation caused by lesions hinder the accurate identification of nerve structures[3–5]. Therefore, there is a need for consistently reliable MRN technology that is effective in both the general population and patients with varying brachial plexopathy for clinical practice.

Although the necessity of intravenous contrast in MRN has raised concern[6], recent studies utilizing gadolinium(Gd)-based contrast agents or supraparamagnetic iron oxide nanoparticles have demonstrated robust vascular suppression and promising clinical potentia[7–9]. By combining the paramagnetic characteristics of contrast agents with the long echo time of fast spin echo (FSE) or turbo spin echo (TSE) sequence, the T2 relaxation

[1]Department of Radiology, Union Hospital, Tongji Medical College, Huazhong University of Science and Technology, No. 1277 Jiefang Avenue, Wuhan 430022, Hubei, China. [2]Hubei Province Key Laboratory of Molecular Imaging, Wuhan 430022, China. [3]Department of Radiology, Yijishan Hospital, Wannan Medical College, No.2 Zheshan West Road, Wuhu 241001, Anhui, China. [4]These author contributed equally: Wenjun Wu and Yuhong Ding. ✉email: wuhan_wuwj@163.com; xilong@hust.edu.cn

times of blood retained in vessels are effectively reduced, resulting in a significant decrease of T2 signal intensity within the vessels, including small veins[7–9]. The efficacy of the contrast-enhanced 3D FSE/TSE short tau inversion recovery (STIR) sequence or contrast-enhanced MRN (CE-MRN) has been substantiated by multiple studies, highlighting its superior visualization capabilities for various nerves and their distal branches, including BP, lumbarsacro plexus, extra-cranial segments of cranial nerves, ulnar and median nerves[3,5,10,11]. Furthermore, a comparative study of various Gd-based contrast agents (Gd-BOPTA, Gd-DTPA, and Gd-DOTA) revealed no discernible difference in the efficacy of imaging BP[12]. Another study utilized a combination of CE-MRN and magnetic resonance angiography to simultaneously assess BP and arterial conditions at one injection, providing more diagnostic insights[13]. CE-MRN based cinematic volume rendering and image merging techniques provided us with a novel perspective for the observation of lesions in or around BP[14]. Hence, CE-MRN exhibits great potential as a imaging modality for visualizing and diagnosing brachial plexopathy.

However, whether CE-MRN can stably improve BP visualization and provide additional imaging features in patients with different brachial plexopathy has not been fully explored. The objective of this study is to conduct a comprehensive qualitative and quantitative comparison of image quality among patients with different brachial plexopathy, while also elucidating the distinct imaging features associated with compression/entrapment, injury, and neoplasias on CE-MRN, thereby providing further evidence to support the clinical application of CE-MRN.

Results

Qualitative evaluation

The inter-reader agreement for nerve visualization scores in each area was found to be consistently high, ranging from good to excellent for both plain MRN (κ = 0.76–0.85) and CE-MRN (κ = 0.80–0.92). In all subjects, the total score of CE-MRN was significantly higher than that of plain MRN ($p < 0.001$, Fig. 1A). Regional scores of CE-MRN were notably superior to those of plain MRN, particularly in the costoclavicular space and axillary region (all $p < 0.05$, Fig. 1B). Across groups, CE-MRN significantly improved the nerve visualization in all regions, especially among volunteers and patients with BP injury (Table 1).

Quantitative assessment

As the representitive nerve of BP in all subjects, the signal intensity of C7 nerve measured on CE-MRN images was found to be lower compared to plain MRN images (116.41 ± 70.39 vs. 131.15 ± 64.73). CE-MRN exhibited a lower CNR (nerve versus muscle) and significantly higher CNR (nerve versus vein), CNR (nerve versus ganglion) and CNR (nerve versus lymph node) than plain MRN (Fig. 1C). Meanwhile, CE-MRN demonstrated significantly higher CR (nerve versus muscle), CR (nerve versus fat), CR (nerve versus Bone marrow), CR (nerve versus vein), CR (nerve versus ganglion) and CR (nerve versus lymph node) than plain MRN (Fig. 1D). Across all

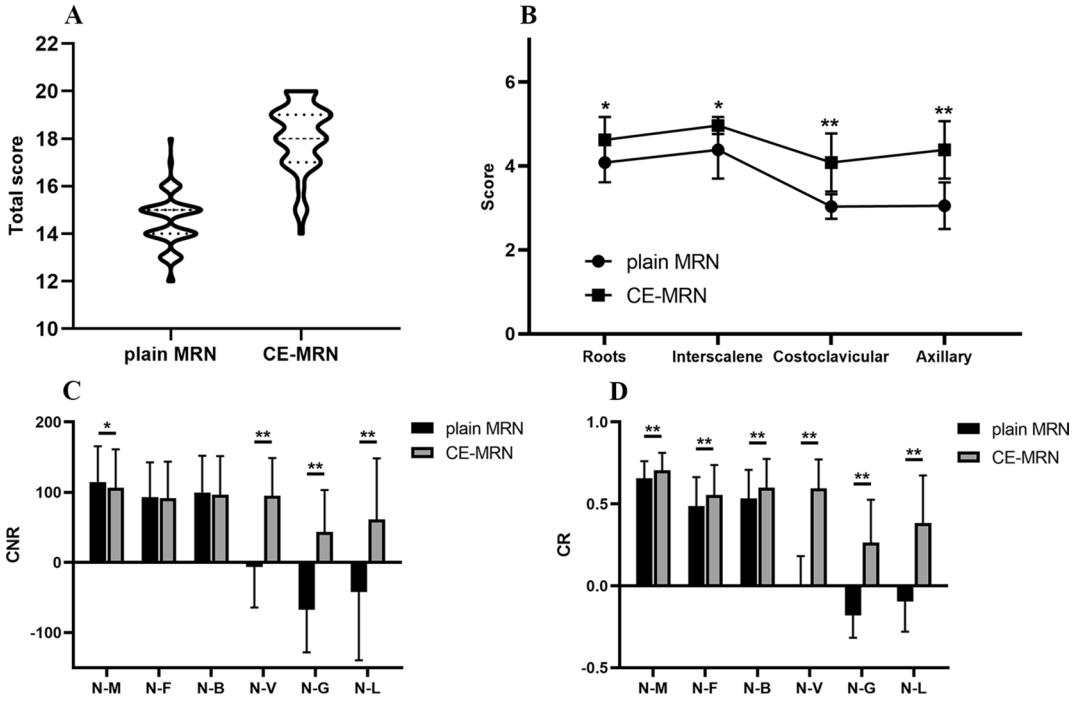

Fig. 1. Qualitative and quantitative evaluation between plain MRN and CE-MRN in all subjects. Comparison of total score (**A**), segmental scores (**B**) for nerve visualization, contrast-to-noise ratio (CNR, **C**) and contrast ratio (CR, **D**) between plain MRN and CE-MRN. N-M = nerve versus muscle, N-F = nerve versus fat, N-B = nerve versus bone marrow, N-V = nerve versus vein, N-G = nerve versus ganglion, N-L = nerve versus lymph node, CNR = contrast-to-noise ratio, CR = contrast ratio, * < 0.05, ** < 0.001.

	Volunteers (n = 19)		Compression/entrapment (n = 9)		Injury (n = 22)		Neoplasia (n = 11)		No identified pathology (n = 10)	
	Plain MRN	CE-MRN	Plain MRN	CE-MRN	Plain MRN	CE-MRN	Plain MRN	CE-MRN	Plain MRN	CE-MRN
Roots	4.00 ± 0.34	4.72 ± 0.57**	4.25 ± 0.46	4.63 ± 0.52	4.00 ± 0.45	4.57 ± 0.51*	4.27 ± 0.47	4.91 ± 0.30*	4.00 ± 0.71	4.56 ± 0.73
Interscalene space	4.50 ± 0.62	4.94 ± 0.24*	4.50 ± 0.53	5.00 ± 0.00*	4.05 ± 0.74	4.95 ± 0.22*	4.45 ± 0.69	4.91 ± 0.30	4.44 ± 0.73	5.00 ± 0.00
Costoclavicular space	2.94 ± 0.24	3.89 ± 0.90*	2.88 ± 0.35	4.13 ± 0.64*	3.05 ± 0.22	4.00 ± 0.63**	3.09 ± 0.30	4.36 ± 0.67*	3.22 ± 0.44	4.33 ± 0.50*
Axillary region	3.00 ± 0.49	4.39 ± 0.61**	3.00 ± 0.54	4.50 ± 0.54*	2.90 ± 0.54	4.33 ± 0.80**	3.36 ± 0.51	4.36 ± 0.81*	3.33 ± 0.71	4.44 ± 0.73*
Total scores	14.44 ± 0.84	17.94 ± 1.39**	14.63 ± 0.74	18.25 ± 1.03*	14.00 ± 1.14	17.86 ± 1.56**	15.18 ± 1.25	18.55 ± 1.51*	15.00 ± 1.12	18.33 ± 1.41*

Table 1. Comparisons of qualitative scores between plain MRN and CE-MRN in volunteers and patients. * < 0.05, ** < 0.001.

groups, there was consistent evidence of increased CNRs and CRs for nerve versus vein, nerve versus ganglion, and nerve versus lymph node. The CRs of nerve versus muscle, nerve versus fat, and nerve versus bone marrow were all higher on CE-MRN than those on plain MRN in both injury and neoplasia groups, when compared to other groups. In the group of patients with no identified pathology, decreased CNRs were observed for nerve versus muscle, nerve versus fat, and nerve versus bone marrow (Table 2).

Normal and pathological findings observed in BP CE-MRN

Typically, the ganglion exhibits a noticeable reduction in signal intensity on CE-MRN images (Fig. 2A,B). The branches of BP, including the suprascapular nerve, musculo-cutaneous nerve, axillary nerve, radial nerve, median nerve and ulnar nerve are more clearly delineated on CE-MRN compared to plain MRN (Fig. 2C,D). In patients with cervical radiculopathy, the continuity of hyperintense preganglion nerve are always interrupted or compressed, showing localized or linear hypointensity at the affected site on CE-MRN (Fig. 3A). In patients with thoracic outlet syndrome, the distorted hperintense nerves can be clearly visualized on CE-MRN. Additionally, the vascular origin can be identified through the use of contrast-enhanced T1 VIBE sequence (Fig. 3B). In patients with BP injury, the pattern can be succinctly classified as traction/crush injury, characterized by continuous nerve course and localized abnormal signal intensity and caliber; nerve rupture, featuring a gap between proximal and distal ends along with nerve retraction and hyperintensity; and roots avulsion accompanied by pseudomeningocele and distal nerve distortion and hyperintensity on CE-MRN (Fig. 4). In patients with neurogenic neoplasias, CE-MRN can precisely visualize the location of the parent nerve, accurately assess neoplasia size and number, and demonstrate a decrease in signal intensity within the enhanced solid component of neoplasias, which is identified as "enhanced target sign" (Fig. 5). The summary of the detailed findings and NS-RADS classification is provided in Table 3.

Discussion

This study investigated the efficacy of CE-MRN in enhancing BP visualization across various diseases and summarized the additional imaging findings. The CE-MRN stably improved the display of BP by eliminating signal contamination from surrounding tissues, including muscles, fat, bone marrow, veins, lymph nodes in both volunteers and patients with nerve compression/entrapment, injury and neoplasias. Compared to other groups, the nerve injury and neoplasia groups demonstrated superior quantitative performance of CE-MRN in increasing tissue contrast, while the volunteer and nerve injury group exhibited superior qualitative performance of CE-MRN in visualizing nerves. The soft tissue edema caused by trauma, mass effect and denervation could be effectively suppressed through the use of paramagnetic contrast agents, resulting in a significant decrease of signal intensity on heavily T2-weighted imaging. The signal decrease of ganglion, the morphological changes in compressed/entrapped nerves, the concise classification of injury, and the "enhanced target sign" of solid neoplasia components should be meticulously observed for accurate diagnosis and evaluation of brachial plexopathy.

MRN has been proposed by Howe since 1990, leading the development of numerous MRI sequences and techniques for peripheral nerve imaging[19]. Due to its complexity and vulnerability, the visualization of BP has garnered significant attention in clinical practice. The top two prerequisites for obtain satisfactory images of BP are high spatial resolution and optimal tissue contrast[1,2]. High-resolution 2D fluid-sensitive sequences and isotropic 3D sequences, combined with fat suppression techniques such as STIR and Dixon, can provide pixel/voxel small enough to depict BP nerves[20,21]. Meanwhile, the perplexing signal from blood vessels of comparable caliber along nerves emerge as the primary impediment to BP imaging. Several non-contrast vascular suppression techniques, such as MSDE, SHINKEI and DW-PSIF utilized preparation pulses of diffusion gradients to dephase rapidly flowing protons in the arteries and large-caliber veins and demonstrated promising efficacy in reducing vascular signal contamination[22–24]. The major concerns of these techniques, however, lie in the insufficient suppression of slow-flowing veins, susceptibility to local field inhomogeneity and motion artifacts[1,2]. Consequently, an alternative approach involves exploring the application of contrast agents to mitigate the interference from small-caliber veins adjacent to nerves.

In recent years, various gadolinium-based contrast agents and a superparamagnetic iron-oxide nanoparticle (ferumoxytol) have been investigated in combination with 3D TSE/FSE STIR sequences for vascular suppression in peripheral nerve MRN[3,9]. These contrast-enhanced technologies, known as CE-MRN, have demonstrated superior visualization of nerves compared to plain scanning, regardless of the presence or absence of non-contrast vascular suppression techniques[5,11,25]. The application of CE-MRN not only effectively suppresses the

	Volunteers (n = 19)		Compression/entrapment (n = 9)		Injury (n = 22)		Neoplasia (n = 11)		No identified pathology (n = 10)	
	Plain MRN	CE-MRN	Plain MRN	CE-MRN	Plain MRN	CE-MRN	Plain MRN	CE-MRN	Plain MRN	CE-MRN
SI										
C7 nerve	98.54 ± 49.88	85.94 ± 42.22	90.79 ± 47.83	80.33 ± 53.48*	166.33 ± 59.45	153.2 ± 86.27	169 ± 72.58	150.1 ± 61.92*	110.39 ± 48.46	88.8 ± 44.75**
CNR										
N vs. M	93.51 ± 41.56	86.86 ± 44.04	85.96 ± 29.4	84.2 ± 44.46	131.78 ± 60.79	122.58 ± 64.79	129.23 ± 48.19	125.95 ± 51.23	126.36 ± 43.03	105.41 ± 51.62*
N vs. F	77.93 ± 46.47	76.27 ± 47.52	62 ± 24.73	64.94 ± 37.53	109.94 ± 57.07	106.78 ± 59.12	104.56 ± 45.44	117.61 ± 38.64	101.89 ± 40.82	82.40 ± 51.66*
N vs. B	83.80 ± 44.28	78.83 ± 46.50	68.2 ± 36.43	72.55 ± 44.47	113.55 ± 57.2	108.97 ± 57.06	115.27 ± 62.56	127.48 ± 61.34	110.98 ± 39.81	91.46 ± 50.37*
N vs. V	− 10.44 ± 55.93	77.17 ± 39.30**	− 29.66 ± 48.06	58.82 ± 25.93**	14.79 ± 52.79	112.18 ± 59**	− 10.5 ± 74.48	122 ± 65.71*	− 19.26 ± 56.85	93.07 ± 47.96*
N vs. G	− 57.95 ± 67.80	48.17 ± 50.62**	− 62.66 ± 28.87	27.36 ± 39.8**	− 67.46 ± 56.85	42.85 ± 78.14**	− 88.65 ± 87.57	53.43 ± 63.79*	− 66.67 ± 42.51	39.92 ± 44.09**
N vs. L	− 21.82 ± 72.38	68.29 ± 49.63**	− 46.52 ± 18.78	33.11 ± 31.44**	− 59.98 ± 129.26	48.18 ± 135.92**	− 53.92 ± 125.97	77.44 ± 55.53*	− 26.26 ± 61.25	84.21 ± 64.03*
CR										
N vs. M	0.66 ± 0.09	0.72 ± 0.07*	0.68 ± 0.07	0.71 ± 0.06	0.66 ± 0.11	0.70 ± 0.12*	0.63 ± 0.13	0.67 ± 0.15*	0.66 ± 0.11	0.71 ± 0.11*
N vs. F	0.49 ± 0.22	0.56 ± 0.24	0.45 ± 0.17	0.52 ± 0.19*	0.49 ± 0.14	0.56 ± 0.13*	0.52 ± 0.22	0.63 ± 0.16*	0.47 ± 0.14	0.48 ± 0.19
N vs. B	0.56 ± 0.19	0.60 ± 0.20	0.5 ± 0.23	0.55 ± 0.19	0.53 ± 0.15	0.60 ± 0.15*	0.52 ± 0.19	0.66 ± 0.17*	0.54 ± 0.14	0.57 ± 0.18
N vs. V	− 0.01 ± 0.19	0.61 ± 0.19**	− 0.08 ± 0.21	0.51 ± 0.19**	0.06 ± 0.17	0.60 ± 0.12**	− 0.001 ± 0.18	0.63 ± 0.24**	− 0.03 ± 0.14	0.60 ± 0.17**
N vs. G	− 0.17 ± 0.18	0.38 ± 0.24**	− 0.23 ± 0.1	0.15 ± 0.27**	− 0.17 ± 0.13	0.26 ± 0.27**	− 0.18 ± 0.13	0.25 ± 0.25**	− 0.17 ± 0.11	0.18 ± 0.22**
N vs. L	− 0.05 ± 0.24	0.48 ± 0.30**	− 0.19 ± 0.09	0.21 ± 0.19**	− 0.11 ± 0.17	0.33 ± 0.30**	− 0.09 ± 0.17	0.37 ± 0.26**	− 0.06 ± 0.14	0.48 ± 0.29**

Table 2. Comparisons of SI, CR, CNR between plain MRN and CE-MRN in volunteers and patients. * < 0.05, ** < 0.001; N vs. M = Nerve versus muscle, N vs. F = Nerve versus fat, N vs. B = Nerve versus bone marrow, N vs. V = Nerve versus vein, N vs. G = Nerve versus ganglion, N vs. L = Nerve versus lymph node, CNR = contrast-to-noise ratio, CR = contrast ratio.

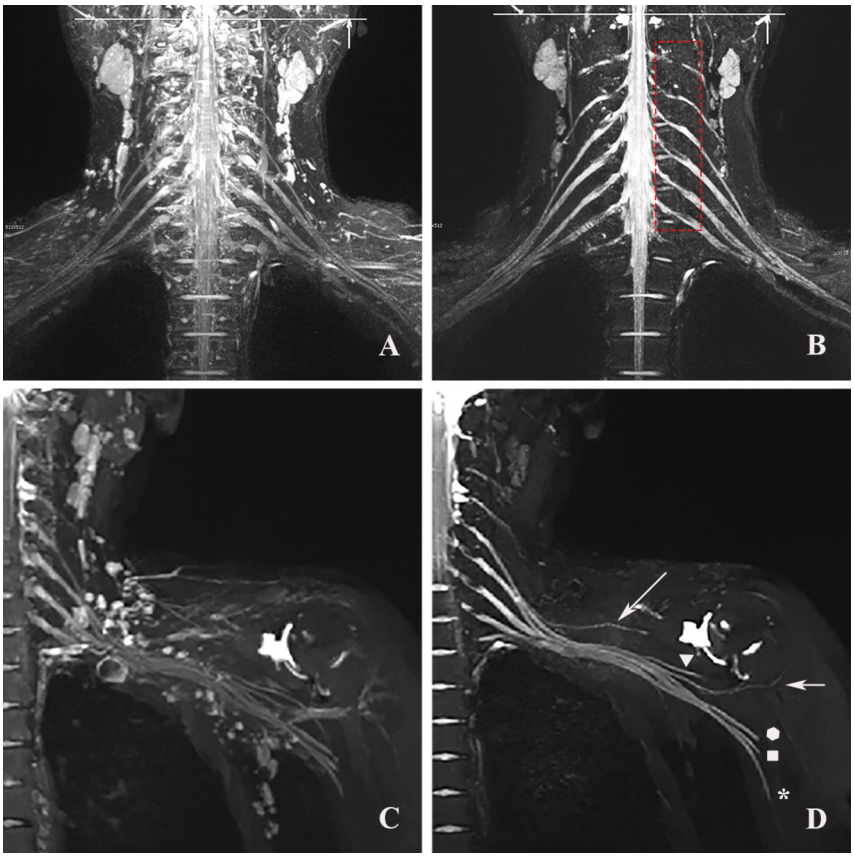

Fig. 2. Representative MIP images of plain MRN (**A**, **C**) and CE-MRN (**B**, **D**) of brachial plexus. CE-MRN effectively mitigates signal contamination from blood vessels and lymph nodes. Ganglia on CE-MRN exhibit hypointensity (**B**, red dotted box). Distal branches including suprascapular nerve (long arrow), musculocutaneous nerve (triangle), axillary nerve (short arrow), radial nerve (hexagon), median nerve (rectangle) and ulnar nerve (star) are more distinctly delineated on CE-MRN (**D**) compared to plain MRN (**C**).

signal of blood vessels, but also demonstrates its efficacy in suppressing the signal of muscles, fat, bone marrow, and lymph nodes[3,11]. Our findings further confirmed that the improvement in BP visualization achieved by CE-MRN was consistent across volunteers and patients with conditions such as nerve compression/entrapment, injury and neoplasia, from both qualitative and quantitative perspectives. The nerve distortion, muscle edema and mass effect did not impede the display of BP; in fact, the visualization of BP might even be further enhanced in patients compared to volunteers.

In a typical CE-MRN, the ganglion exhibited localized T2 weighted hypointensity attributed to compromised blood-nerve barrier (BNB) and subsequent infiltration of contrast agents into the nerve parenchyma. The appearance should be distinguished from the protruded intervertebral disc that is compressing the nerve. The visualization improvement of BP cords and branches, including those in the costoclavicular space and axillary region, was superior to that of the proximal portions on CE-MRN[7]. In compression/entrapment cases, the involved nerve typically exhibits manifestations such as distortion, displacement, changes in caliber and alterations in signal[26–28]. The nerves were always observed to be enlargement with increased signal intensity on T2-weighted MR sequences, including plain MRN, indicative of swelling, degeneration and local inflammation[4,26,27]. However, in cases such as cervical radiculopathy, the nerves on CE-MRN occasionally exhibited a reduction in diameter and a decrease of signal intensity or even disruption at the site of compression. We attributed this phenomenon to the proliferation of granulation tissue, neovascularization and neurofibrosis, or the breakdown of BNB caused by the protruded intervertebral disc. This localized signal decrease sign can serve as an indicator for detecting compression.

The involvement of nerves in injury cases is always accompanied by soft tissue edema and muscle denervation as well as to vascular signal contamination, which hinders the accurate identification of the location, extent and number of injuries using routine MR sequences and plain MRN[22,29]. Conversely, on CE-MRN images, the influx of contrast agent into the soft tissues due to the initial damage along with adjunct hyperemia and venous congestion significantly diminishes the signal of non-nerve soft tissue. Consequently, CE-MRN enables better demarcation of the affected nerve as compared to plain MRN. The BP injury could be easily classified using CE-MRN as follows: crush/traction injury with a continuous appearance but abnormal increased signal, rupture with a gap between proximal and distal ends along with distal Wallerian degeneration, roots avulsion with

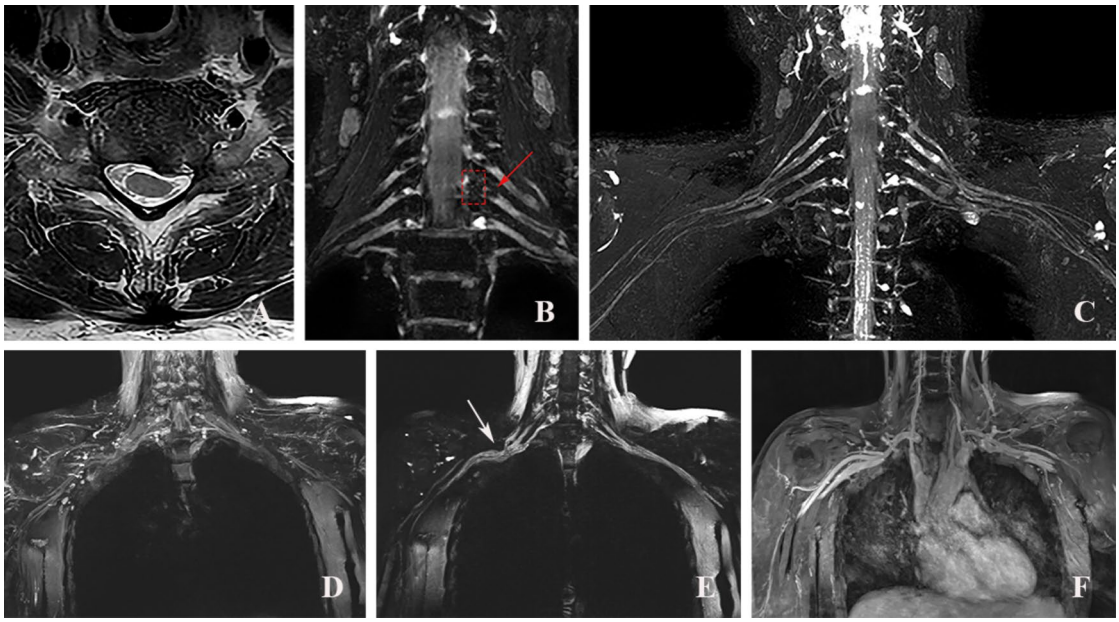

Fig. 3. Representative images of cervical radiculopathy (**A**–**C**) and thoracic outlet syndrome (**D**–**F**). A case with left C6/7 disc herniation on an axial T2-weighted image (**A**) shows localized hypointensity of left C7 preganglion nerve root on a 10 mm MIP CE-MRN image (**B**, red rectangle box) and a full-thickness MIP image (**C**), which should be distinguished from the hypointense ganglion (**B**, red arrow). Another case with right thoracic outlet syndrome shows evident distortion, increased signal intensity of nerves on CE-MRN image (**E**, white arrow) compared to plain MRN image (**D**), accompanied by a sunken subclavian artery on contrast-enhanced T1 VIBE scanning (**F**).

pseudomeningocele and disconnection from the hyperintense shrunken distal nerve, which generally corresponds to the Seddon and Sunderland classifications[30]. The concise CE-MRN classification of BP injury could be used for evaluating the severity of injury and assisting in treatment planning. In neoplasia cases, the assessment of both solitary and multiple neoplasms could be effectively conducted using plain MRN and CE-MRN[31,32]. In addition to tail sign, split fat sign, and fascicular sign on conventional MRI and plain MRN images, the enhanced solid components of the neoplasia exhibited decreased signal on CE-MRN images. This feature could be identified as the "enhanced target sign" in neoplasias such schwannoma and neurofibromatosis. The continuity of nerve could be abruptly interrupted at the neoplasia site due to the significant decrease in signal. Therefore, CE-MRN contributed to identification and diagnosis of peripheral nerve neoplasias by exhibiting the enhancing features.

Recently, Chhabra A et al. have proposed a standardized framework (NS-RADS) for reporting peripheral neuropathies, which is an established and validated system in clinical practice that offers practicality and comprehensibility[15–18]. Our study demonstrated the high suitability of this system for rapid evaluation of various brachial plexopathy including cervical radiculopathy, thoratic outlet syndrome, space-occupying lesion compression, nerve injury, and neurogenic neoplasias. As far as we are concerned, the localized signal decrease sign of compressed nerve might be valuable for evaluating the severity of cervical radiculopathy. The presence of "enhanced target sign" in neurogenic neoplasias could potentially aid in scoring neoplasia. While roots avulsion can be categorized as I-5, a more detailed subclassification that takes into account clinical and pathological characteristics, as well as specialized treatment, would enhance the precision of the system.

We acknowledge the limitations of this study, including a relatively small sample size that prevented thorough evaluation of BP pathologies based on the CE-MRN images. Additionally, as a retrospective analysis, we did not compare the imaging efficacy between CE-MRN and non-contrast vascular suppression techniques such as iMDSE and SHINKEI. Finally, while the scanning time of CE-MRN was relatively long in this study, advanced techniques such as simultaneous multislice acceleration, compressed sensing and deep learning reconstruction could optimize it[33–35].

In conclusion, the visualization improvement of CE-MRN in patients, particularly those with injury and neoplasia, was found to be even more pronounced than that observed in volunteers. The additional imaging features provided by CE-MRN aided in identifying normal morphology and detecting and evaluating of BP pathologies. Therefore, CE-MRN is an ideal imaging modality for selectively visualizing the BP and facilitating clinical diagnosis and treatment decisions for various BP-related diseases.

Methods

Subjects

This study was conducted in accordance with the principles outlined in the Declaration of Helsinki. Ethical approval for this study was obtained from the Ethics Committee of Union Hospital, Tongji Medical College, Huazhong University of Science and Technology (No. UHCT21809, approval date 2021-01-04), and informed consent was obtained from all participants including volunteers and patients. A convenient sampling approach

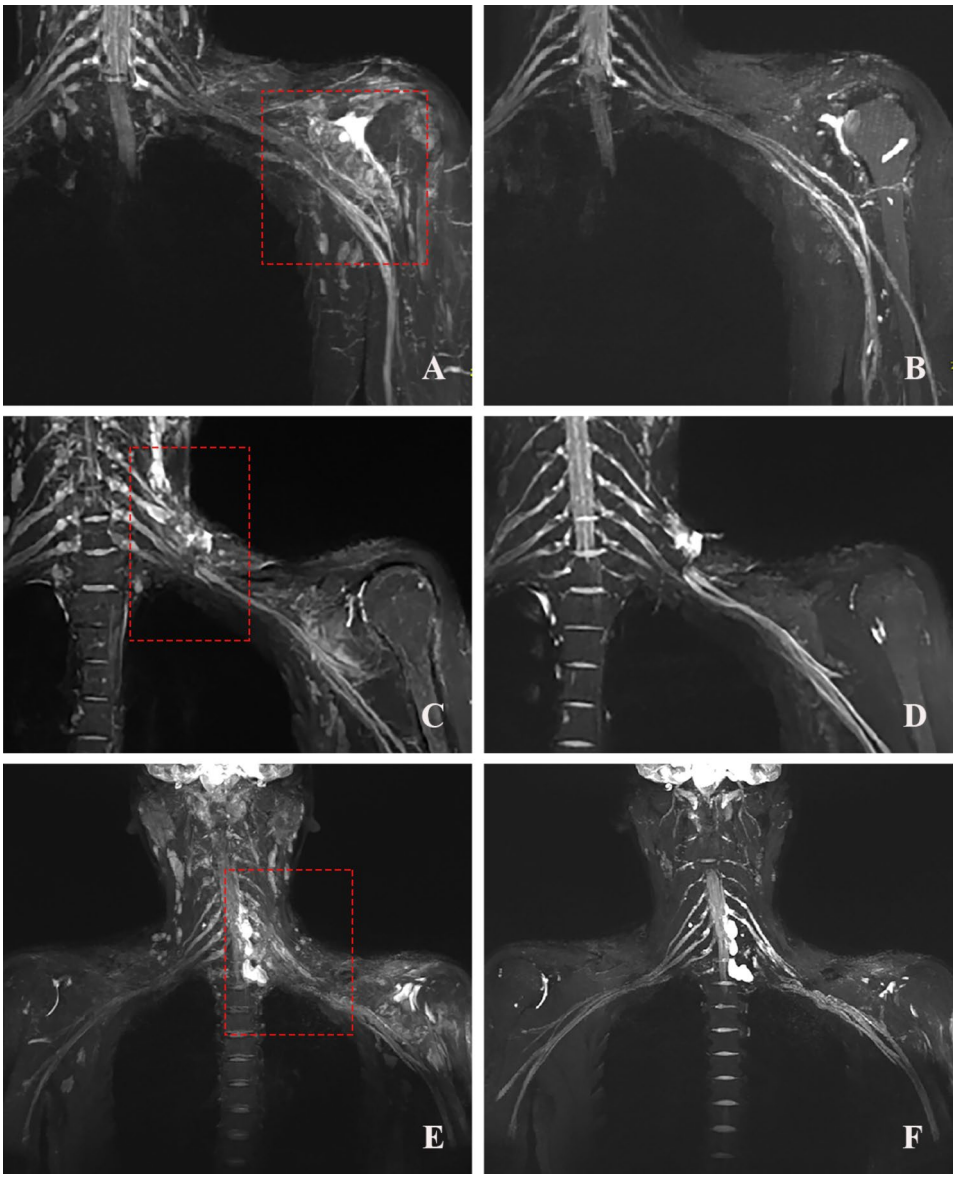

Fig. 4. Representative images depicting three different types of brachial plexus injury. First case of acute crush injury in the axillary region exhibits indistinct nerves affected by muscle edema on a plain MRN image (**A**, red rectangle box), while nerve branches with increased signal intensity are clearly visible on a CE-MRN image (**B**). Second case with an incise injury at the interscalene level demonstrates an indistinct continuity of nerves, which is obscured by muscle edema and hemorrhage on a plain MRN image (**C**), while a definite disruption of C5 and C6 nerves along with distal nerve hypertrophy and hyperintensity is observed on a CE-MRN image (**D**). Third case with roots avulsion exhibits pseudomeningocele and indistinct nerve structure on a plain MRN image (E), while apparent C7-T1 pseudomeningoceles and disconnection from distal hyperintense nerves, along with hyperintense C5–C6 nerve trunks and a discontinuity at the costoclavicular level are revealed on a CE-MRN image (**F**).

was use for subjects recruitment. From July 2021 through May 2023, nineteen healthy volunteers (11 female and 8 male; median age, 39 years; age range, 17–66 years) were recruited from university students and hospital staff, while fifty-two patients (23 female and 29 male; median age, 40 years; age range, 11–72 years) were enrolled in this study. The inclusion criteria for patients encompassed complaints of cervical, scapular, and brachial symptoms such as pain, numbness, dysesthesia, fatigue, motor deficit, muscle wasting, presence of mass or history of trauma. The exclusion criteria comprised the following: (1) individuals with any MRI contraindications; (2) individuals who expressed unwillingness or inability to complete MRI examinations; (3) individuals whose images exhibited severe artifacts, rendering them unsuitable for diagnostic purposes due to poor image quality. After clinical and radiological diagnosis, there were 9 cases of nerve compression/entrapment, 22 cases of nerve injury, 11 cases of neurogenic neoplasia, and 10 cases without brachial plexopathy identified. Finally, this study included a total of 71 subjects.

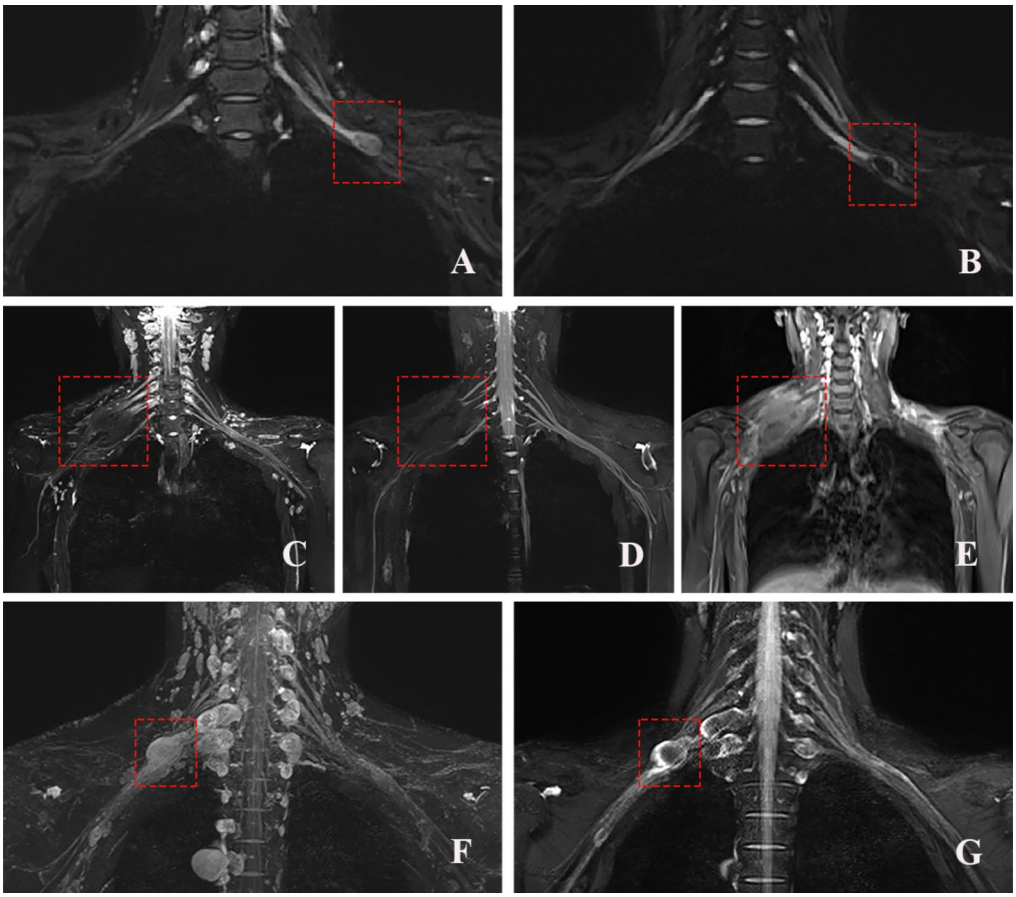

Fig. 5. Representative images illustrating three different forms of brachial plexus neoplasia. First case of schwannoma presents a neurogenic, inhomogeneous hyperintense nodule on a plain MRN image (**A**, red rectangle box), while an evident central signal decrease is revealed as "enhanced target sign" on a CE-MRN image (**B**). Second case of neurofibroma demonstrates a diffuse hypointense mass along nerves on a plain MRN image (**C**), with moderate inhomogeneous enhancement on a contrast enhanced T1 VIBE image (**E**). Additionally, regional signal decrease and an abrupt disruption are observe on a a CE-MRN image (**D**). Third case of neurofibromatosis exhibits multiple masses arranged in a nerve distribution pattern on a plain MRN image (**F**), while multiple "enhanced target signs" are observed on a CE-MRN image (**G**, red rectangle box).

MR imaging protocol

All subjects underwent examination on a 3.0 T MR unit (Trio, Siemens Medical Solutions, Erlangen, Germany). A combination of a 6-channel body coil, a 6-channel neck coil, and a 6-channel spine coil was used to cover the whole BP. The MRI protocol included axial T1-weighted TSE, coronal T2-wighted TSE STIR, coronal T1-weighted 3D volumetric interpolated body examination (VIBE) and coronal T2-weighted 3D sampling perfection with application optimized contrast using different flip angle evolution (SPACE) STIR sequences. The 3D VIBE and 3D SPACE STIR sequences were acquired both pre- and post-injection of gadobenate dimeglumine (MultiHance, Bracco Imaging). The Gd-based contrast was administered at a dose of 0.3 ml/kg was injected through an indwelling venous catheter at a speed of 1.5 ml/s.

The parameters for the axial T1-weighted TSE, coronal T2-wighted TSE STIR and coronal 3D VIBE sequences were as following: TR/TE = 600/20 ms, FOV = 380 × 380 mm^2, slice thickness = 5 mm, slice number = 30; TR/TE/TI = 4000/39/220 ms, FOV = 448 × 448 mm^2, matrix = 384 × 384, slice thickness = 5 mm, slice number = 20; TR/TE = 8.18/3.04 ms, FOV = 448 × 448 mm^2, matrix = 448 × 448, slice thickness = 1.2 mm, slice number = 120, bandwidth, 130 Hz/Px, iPAT acceleration factors = 2, acquisition time = 2 min 4 s.

The coronal 3D SPACE STIR imaging was acquired using the specified parameters: TR/TE/TI = 4000/286/220 ms, ETL = 157, FOV = 448 × 448 mm^2, matrix = 448 × 448, slice thickness = 1 mm, slice number = 120, voxel resolution = 1 × 1 × 1 mm^3, NEX = 1.8, iPAT acceleration factor = 2, acquisition time = 10 min 50 s.

Qualitative evaluation

The original plain MRN and CE-MRN images were anonymized and evaluated by two radiologists (W.W. with 8 years experience, and Y.D. with 8 years experience) who were blinded to the information of subjects on a PACS workstation (Carestream, Shanghai, China). Image post-processing techniques, including maximum intensity projection (MIP) and multiplanar reconstruction reformatter (MPR), were employed to generate 3D views of

	Category (number)	NS-RADS (number)	Conventional imaging manifestations	Additional imaging features on CE-MRN
Nerve compression/entrapment (N = 9)	Cervical radiculopathy (n = 6)	E-2 (n = 2) E-3 (n = 4)	Disc herniation and foraminal stenosis on routine T1 and T2 weighted imaging. Increased signal, narrowing at compression site, proximal and/or distal enlargement of nerve on plain MRN	Localized hypointensity or decreased extent of normal hyperintensity at the compression site of the preganglion nerve
	Thoratic outlet syndrome (n = 2)	E-2 (n = 2)	Disappearance of the fat space between the normal structure on routine MRI. Kink of the affected nerve segment on plain MRN	Distorted course of the compressed nerve without vascular signal contamination Reconstructed MRA using contrast-enhanced T1 VIBE images for identifying vascular origin
	Space-occupying lesion (n = 1) (Pseudoaneurysm)	E-1 (n = 1)	Mass effect and abnormal signal of the lesion without clear differentiation of nerves on routine images and plain MRN	Displacement and deformation of compressed nerves and signal increase of distal nerves
Nerve injury (N = 22)	Nerve crush/traction injury (n = 10)	I-2 (n = 2) I-3 (n = 8)	Localized abnormal signal with inadequate nerve visualization on routine MRI. Localized nerve swelling and signal increase, and distal nerve signal increase on plain MRN	Localized nerve swelling and signal increase with better background signal suppression
	Nerve rupture (n = 5)	I-5 (n = 5)	Localized structural disarrangement and abnormal signal with suspecious disconnection of nerve continuity on routine MRI. Unclear gap between the proximal and distal ends with regional soft tissue edema and hematoma or scar tissue on plain MRN	Definitive interruption of nerve continuity, retraction of proximal and distal nerves, and nerve swelling with increased signal intensity
	Nerve roots avulsion (n = 7)	I-5 (n = 7)	Nerve rootlets avulsion on MR myelography, pseudomeningocele and surrounding abnrmal signal on routine MRI; pseudomeningocele, soft tissue edema and unclear nerve disconnection on plain MRN	Pseudomeningocele, definitive nerve disconnection and distal nerve retraction, swelling and signal increase
Nerve neoplasia (n = 11)	Schwannoma (n = 7)	N-1 (n = 7)	Well-defined (encapsulated) mass displacing the nerve fascicles with split fat sign, target sign, fascicular sign, tail sign on routine MRI and plain MRN	Signal decrease of solid enhanced component, with an edge or central hyperintense area, manifests as "enhanced target sign" occasionally
	Neurofibroma (n = 2)	N-2 (n = 2)	Nerve fascicle-infiltrating mass with split fat sign, target sign, fascicular sign, tail sign on routine MRI and plain MRN	Signal decrease of solid enhanced components more diffusely, Pseudodisruption of the nerves
	Neurofibromatosis (n = 2)	N-2 (n = 2)	Multiple masses with split fat sign, target sign, fascicular sign, tail sign on routine MRI and plain MRN	Signal decrease of solid enhanced components, and simultaneous display of multiple masses and nerves

Table 3. Category and comparison of imaging findings on routine MRI, plain MRN and CE-MRN.

the BP. The nerve display in the roots, interscalene space, costoclavicular space, and axillary region were scored using a 5-point scale, respectively: (1) absence of identifiable nerve course; (2) presence of identifiable nerve course but with severe signal contamination from veins, lymph nodes, muscles, fat, etc.; (3) presence of identifiable nerve course with unclear boundary and moderate signal contamination; (4) presence of identifiable nerve course with clear boundary and mild signal contamination; (5) well depicted nerve course with high contrast and no signal contamination. The final score was determined by a senior neuroradiologist (X.L. with 12 years of experience) in the absence of unanimous agreement on the qualitative evaluation. The overall score for each case was calculated by summing up the scores from the four areas. The normal morphology, compression/entrapment, injury, and neoplasias of BP were classified based on the clinical and radiological characteristics. Additionally, all nerve lesions were classified according to the Neuropathy Score Reporting and Data System (NS-RADS)[15–18], with further investigation of their manifestation on CE-MRN images.

Quantitative measurement

The healthy side of C7 nerve root and its adjacent tissue (e.g., scalene muscle, fat tissue surrounding supraclavicular nerves, 6th cervical vertebra body, supraclavicular vein, C7 ganglion and cervical lymph node), and surrounding air were selected as regions of interest (ROIs) for acquiring tissue signal intensity (SI) and background noise standard deviation (SD). These measurements were made by a radiologist (W.W.). The ROIs were delineated on the plain MRN and CE-MRN source images on a post-processing workstation (Syngo, Siemens, Germany). Contrast-to-noise ratio (CNR), and contrast ratio (CR) were calculated for all subjects. These metrics were subsequently compared between plain MRN and CE-MRN in both volunteers and patients, separately. The formulas utilized for calculating CNR and CR were as follows:

$$CNR = (SI_{nerve} - SI_{tissue})/SD_{air} \quad (1)$$

$$CR = (SI_{nerve} - SI_{tissue})/(SI_{nerve} + SI_{tissue}) \quad (2)$$

in which "$_{tissue}$" represents other tissues (e.g., muscle, fat, bone marrow, vein, ganglion and lymph node) .

Statistical analysis

All data were expressed as average ± standard deviation (SD). For qualitative data, inter-reader agreement of nerve visualization scoring on both plain MRN and CE-MRN was assessed using weighted Cohen's Kappa analysis, with the following interpretation: 0.81–1.00: Excellent, 0.61–0.80: Good, 0.41–0.60: Moderate, 0.21–0.40: Fair, and 0.00–0.20: Slight. Wilcoxon signed-rank test was used to compare the differences of the scores between plain MRN and CE-MRN in both overall and distinct groups. For quantitative data, a paired t-test was used to compare differences of image measurements between plain MRN and CE-MRN in both overall and distinct groups. All statistical analyses were performed using software SPSS 26.0 (SPSS, Inc, Chicago, IL, USA). A p value < 0.05 was used to determine statistical significance.

Data availability

The data that support the findings of this study are available from the corresponding authors on reasonable request.

Received: 17 June 2024; Accepted: 28 August 2024
Published online: 05 September 2024

References

1. Jung, J. Y., Lin, Y. & Carrino, J. A. An updated review of magnetic resonance neurography for plexus imaging. *Korean J. Radiol.* **24**(11), 1114–1130 (2023).
2. Davidson, E. J., Tan, E. T., Pedrick, E. G. & Sneag, D. B. Brachial plexus magnetic resonance neurography: Technical challenges and solutions. *Investig. Radiol.* **58**(1), 14–27 (2023).
3. Wang, L. X. *et al.* The application of paramagnetic contrast-based T2 effect to 3D heavily T2W high-resolution MR imaging of the brachial plexus and its branches. *Eur. J. Radiol.* **85**(3), 578–584 (2016).
4. Gilcrease-Garcia, B. M., Deshmukh, S. D. & Parsons, M. S. Anatomy, imaging, and pathologic conditions of the brachial plexus. *Radiograph. Rev. Public. Radiol. Soc. North Am.Inc.* **40**(6), 1686–1714 (2020).
5. Kang, J. *et al.* Improved visualization of median, ulnar nerves, and small branches in the wrist and palm using contrast-enhanced magnetic resonance neurography. *Ther. Adv. Neurol. Disord.* https://doi.org/10.1177/17562864241239739 (2024).
6. Harrell, A. D., Johnson, D., Samet, J., Omar, I. M. & Deshmukh, S. With or without? A retrospective analysis of intravenous contrast utility in magnetic resonance neurography. *Skelet. Radiol.* **49**(4), 577–584 (2020).
7. Sneag, D. B. *et al.* Post-contrast 3D inversion recovery magnetic resonance neurography for evaluation of branch nerves of the brachial plexus. *Eur. J. Radiol.* **132**, 109304 (2020).
8. Queler, S. C., Tan, E. T., Geannette, C., Prince, M. & Sneag, D. B. Ferumoxytol-enhanced vascular suppression in magnetic resonance neurography. *Skelet. Radiol.* **50**(11), 2255–2266 (2021).
9. Pedrick, E. G., Sneag, D. B., Colucci, P. G., Duong, M. & Tan, E. T. Three-dimensional MR neurography of the brachial plexus: vascular suppression with low-dose ferumoxytol. *Radiology* **307**(1), e221087 (2023).
10. Zhang, Y. *et al.* Enhanced MR neurography of the lumbosacral plexus with robust vascular suppression and improved delineation of its small branches. *Eur. J. Radiol.* **129**, 109128 (2020).
11. Wu, W. *et al.* Visualization of the morphology and pathology of the peripheral branches of the cranial nerves using three-dimensional high-resolution high-contrast magnetic resonance neurography. *Eur. J. Radiol.* **132**, 109137 (2020).
12. Zhang, X., Wang, W., Liu, T., Qi, Y. & Ma, L. The effects of three different contrast agents (Gd-BOPTA, Gd-DTPA, and Gd-DOTA) on brachial plexus magnetic resonance imaging. *Ann. Transl. Med.* **9**(4), 344 (2021).
13. Xu, Z. *et al.* Combine contrast-enhanced 3D T2-weighted short inversion time inversion recovery MR neurography with MR angiography at 1.5 T in the assessment of brachial plexopathy. *MAGMA* **34**(2), 229–239 (2021).
14. Chen, R. *et al.* The value of the cinematic volume rendering technique: Magnetic resonance imaging in diagnosing tumors associated with the brachial plexus. *Eur. J. Med. Res.* **28**(1), 569 (2023).
15. Chhabra, A. *et al.* Neuropathy score reporting and data system: A reporting guideline for MRI of peripheral neuropathy with a multicenter validation study. *AJR Am. J. Roentgenol.* **219**(2), 279–291 (2022).
16. Chhabra, A. *et al.* Neuropathy score reporting and data system (NS-RADS): MRI reporting guideline of peripheral neuropathy explained and reviewed. *Skelet. Radiol.* **51**(10), 1909–1922 (2022).
17. Chhabra, A. *et al.* MRI-based neuropathy score reporting and data system (NS-RADS): multi-institutional wider-experience usability study of peripheral neuropathy conditions among 32 radiology readers. *Eur. Radiol.* https://doi.org/10.1007/s00330-023-10517-2 (2024).
18. Taneja, A. K. & Chhabra, A. Neuropathy score reporting and data system (NS-RADS): A practical review of mri-based peripheral neuropathy assessment. *Semin. Ultrasound CT MR* **44**(4), 386–397 (2023).
19. Howe, F. A., Filler, A. G., Bell, B. A. & Griffiths, J. R. Magnetic resonance neurography. *Magn. Reson Med.* **28**(2), 328–338 (1992).
20. Chen, W. C. *et al.* Value of enhancement technique in 3D-T2-STIR images of the brachial plexus. *J. Comput. Assisted Tomograp.* **38**(3), 335–339 (2014).
21. Wang, X. *et al.* MR neurography of brachial plexus at 3.0 T with robust fat and blood suppression. *Radiology* **283**(2), 538–546 (2017).
22. Zhang, Y. *et al.* 3D SHINKEI MR neurography in evaluation of traumatic brachial plexus. *Sci. Rep.* **14**(1), 6268 (2024).
23. Dos Santos, S. J. *et al.* "Million dollar nerve" magnetic resonance neurography: first normal and pathological findings. *Eur. Radiol.* **32**(2), 1154–1162 (2022).
24. Klupp, E. *et al.* Improved brachial plexus visualization using an adiabatic iMSDE-prepared STIR 3D TSE. *Clin. Neuroradiol.* **29**(4), 631–638 (2019).
25. Casselman, J. *et al.* 3D CRANI, a novel MR neurography sequence, can reliable visualise the extraforaminal cranial and occipital nerves. *Eur. Radiol.* **33**(4), 2861–2870 (2023).
26. Schwarz, D. *et al.* Diagnostic value of magnetic resonance neurography in cervical radiculopathy: Plexus patterns and peripheral nerve lesions. *Investig. Radiol.* **53**(3), 158–166 (2018).
27. Yoshida, T., Sueyoshi, T., Suwazono, S. & Suehara, M. Three-tesla magnetic resonance neurography of the brachial plexus in cervical radiculopathy. *Muscle Nerve* **52**(3), 392–396 (2015).

28. Magill, S. T., Brus-Ramer, M., Weinstein, P. R., Chin, C. T. & Jacques, L. Neurogenic thoracic outlet syndrome: current diagnostic criteria and advances in MRI diagnostics. *Neurosurg. Focus* **39**(3), E7 (2015).
29. Leigheb, M. *et al.* Diagnostic accuracy of the magnetic resonance imaging in adult post-ganglionic brachial plexus traumatic injuries: A systematic review and meta-analysis. *Brain Sci.* **11**(2), 173 (2021).
30. Noland, S. S., Bishop, A. T., Spinner, R. J. & Shin, A. Y. Adult traumatic brachial plexus injuries. *J. Am. Acad. Orthop. Surg.* **27**(19), 705–716 (2019).
31. Zhai, H., Lv, Y., Kong, X., Liu, X. & Liu, D. Magnetic resonance neurography appearance and diagnostic evaluation of peripheral nerve sheath tumors. *Sci. Rep.* **9**(1), 6939 (2019).
32. Chhabra, A. *et al.* Anatomic MR imaging and functional diffusion tensor imaging of peripheral nerve tumors and tumorlike conditions. *AJNR Am. J. Neuroradiol.* **34**(4), 802–807 (2013).
33. Preisner, F. *et al.* Simultaneous multislice accelerated TSE for improved spatiotemporal resolution and diagnostic accuracy in magnetic resonance neurography: A feasibility study. *Investig. Radiol.* **58**(5), 363–371 (2023).
34. Hu, S. X. *et al.* Accelerated 3D MR neurography of the brachial plexus using deep learning-constrained compressed sensing. *Eur. Radiol.* **34**(2), 842–851 (2024).
35. Sneag, D. B. *et al.* Optimized 3D brachial plexus MR neurography using deep learning reconstruction. *Skelet. Radiol.* **53**(4), 779–789 (2024).

Author contributions

W. W Conceptualization, Data curation, Formal analysis, Funding acquisition, Investigation, Methodology, Resources, Software, Validation, Visualization, Writing—original draft D. Y Conceptualization, Data curation, Formal analysis, Investigation, Methodology, Software, Visualization, Writing—original draft S. Y Data curation, Methodology, Software, Writing—review & editing W. Y Data curation, Investigation, Software, Writing—review & editing L. T Data curation, Investigation, Software, Writing—review & editing L. D Methodology, Software, Writing—review & editing L. C Data curation, Investigation, Methodology, Visualization, Writing—review & editing Z. C Resources, Software, Supervision, Writing—review & editing W. L Conceptualization, Funding acquisition, Investigation, Methodology, Project administration, Resources, Supervision, Validation, Writing—review & editing L. X Conceptualization, Data curation, Investigation, Project administration, Resources, Software, Supervision, Validation, Writing -review & editing.

Funding

Hubei Province key research and development project (2022BCA034) . Scientific Research Foundation of Wuhan Union Hospital (02.03.2018–224, 02.03.2019–131, F016.02004.21003.103).

Competing interests

The authors declare no competing interests.

Additional information

Correspondence and requests for materials should be addressed to W.W. or X.L.

Reprints and permissions information is available at www.nature.com/reprints.

Publisher's note Springer Nature remains neutral with regard to jurisdictional claims in published maps and institutional affiliations.